Check for updates

Tunable sequential pathways through spatial partitioning and frustration tuning in soft metamaterials†

Asma El Elmi and Damiano Pasini ⓘ *

Elastic instabilities have been leveraged in soft metamaterials to attain novel functionalities such as mechanical memory and sequential pathways. Pathways have been realized in complex media or within a collection of hysteretic elements. However, much less has been explored in frustrated and partitioned soft metamaterials. In this work, we introduce spatial partitioning as a method to localize deformation in sub-regions of a large and soft metamaterial. The partitioning is achieved through the strategic arrangement of soft inclusions in a soft lattice, which form distinct regions behaving as mechanical units. We examine two partitions: an *equally spaced layer partition* with mechanical units connected in series, and a *cross partition*, represented by interconnected series of mechanical units in parallel. Sequential pathways are obtained by frustrating the partitioned metamaterial post-manufacture and are characterized by tracking the polarization change in each partition region. Through a combination of experiments and simulations, we demonstrate that partitioning enables tuning the pathway from longitudinal with weak interactions to a pathway exhibiting strong interactions rising from geometric incompatibility and central domain rotation. We show that tuning the level of uniform lateral pre-strain provides a wide range of tunability from disabling to modifying the sequential pathway. We also show that imposing a nonuniform confinement and altering the tilting of one or two of the domain edges enables to program the pathway, access a larger set of states, and tune the level of interaction between the regions.

1. Introduction

Mechanical metamaterials can expand the range of properties and functionalities offered by conventional materials. Of interest, here, are elastic instabilities in soft metamaterials[1–4] that have been leveraged to elicit transition waves[5–9] and large reversible deformation.[10–12] When triggered, elastic instabilities can make the metamaterial switch between multiple stable, or metastable states,[13] which can be utilized to encode and process information[14–16] and to form sequential pathways.[17–20]

Multistep pathways in complex media often show hysteresis caused by abrupt readjustments in their internal architecture.[17,18] As a result, their state depends on the history of the driving field and the state transitions experienced by the system. A collection of state transitions is often modeled as a system of hysteretic elements with two-state degrees of freedom,[20,21] namely hysterons. Under a change of a driving field, U, the system can undergo a binary behavior: an increase to a given threshold U^+ makes the

system switch from state 0 to 1, whereas a decrease to a threshold U^- leads to a switch from state 1 to 0. If $U^- < U^+$, the transition is hysteretic, and the state of the element for a driving field between the two thresholds can only be determined by tracking the deformation history.[13] In the absence of coupling, a collection of hysterons exhibit Preisach pathways.[21–23]

Interactions between hysterons have been studied numerically, showing avalanches and transient memories.[24–26] Experimentally, their control and tuning, have been a challenge, especially in disordered systems such as crumpled sheets[27–29] and amorphous media.[27,30,31] Only recently has the tuning of sequential pathways been studied under compression in corrugated sheets[20] leading to Preisach[18,20] and scrambled pathways.[20] Sequential pathways have also been studied lately in a complex system of bistable beams embedded in a biholar lattice[32,33] (*i.e.*, a periodic arrangement of alternating small and large holes in a 2D rubbery slab) interacting with pushers.[18] The attainment of the sequential pathways, in these studies,[18,20] has been accomplished by manipulating the geometry of the hysterons, which are organized in parallel. However, not much has been realized to attain sequential pathways in a large soft metamaterial featuring series, or complex arrangement of hysterons, subsequent to its fabrication. This area remains unchartered, yet a rich territory to explore

Department of Mechanical Engineering, McGill University, 817 Sherbrooke St. West, H3A 0C3 Montréal, Québec, Canada. E-mail: damiano.pasini@mcgill.ca

despite some challenges attributed to uncontrollable geometry, resulting in additional degrees of freedom, and to the challenge of experimentally characterizing and tuning hysterons properties.

In this work, we present spatial partitioning as a simple yet effective method to localize deformation and create mechanical clusters in a large soft metamaterial domain. We focus on the biholar lattice and partition it by embedding soft inclusions at specific locations departing from periodicity. Two partitions are examined. The first, namely *equally spaced layer partition*, consists of two evenly spaced layers of soft inclusions that are in series. The second, *cross partition*, comprises soft inclusions embedded in the form of a cross, hence creating interconnected series of mechanical units connected in parallel.

To obtain a hysteretic response in the metamaterial regions, we generate frustration post-manufacture by applying a combination of lateral confinement[33] and tilting. We experimentally determine the states of the metamaterial regions by tracking the polarization in individual regions of the domain. We find that spatial partitioning of frustrated metamaterials enables sequential pathway tuning from a longitudinal pathway with weak interactions to a pathway displaying strong interactions arising from geometric incompatibility and internal rotation. Our work shows that a post-manufacturing strategy that uses lateral confinement and angle tuning of one or two of the clamping edges enables tuning the pathway and the intensity of regions' interaction.

2. Biholar domain, soft inclusion patterns, and applied loadings

We start by defining our domain, a biholar lattice,[32,33] consisting of a 2D rubber array of alternating large and small circular holes with diameters $D_1 = 10$ mm and $D_2 = 7$ mm (Fig. 1a). The effective dimensions are W and H, with $n_W = 9$ and $n_H = 11$ denoting the number of holes in the horizontal and vertical directions, and $P = 10$ mm the distance between the centers of the holes. When combined, it yields $W = P(n_W - 1) + D_1$ and $H = P(n_H - 1) + D_1$. We extend the upper and lower boundaries by $P/2$ (Fig. 1a) simply to ensure a uniform application of the loading at the top and bottom of the sample. The structure is characterized by biholarity $X = \dfrac{D_1 - D_2}{P} = 0.3$ and filaments thickness $t = 1.5$ mm.

As per the loading application and sequence, we first constraint the domain horizontally by imposing a horizontal strain $\varepsilon_x = \dfrac{L_x - L_{x_0}}{L_{x_0}}$ (horizontal arrows in Fig. 1b) where L_x and L_{x_0} represent the current and the initial distance between the sides of even rows, respectively (Fig. 1a). We then apply a uniaxial compression–decompression loading in the form of ε_y (vertical arrows in Fig. 1b). One goal of this work is to investigate the unexplored distributions of soft inclusions, beyond ensembles of parallel connections, that can lead to complex arrangements of interacting hysterons. To create soft inclusions, we simply fill selected holes in the periodic lattice with our base material,
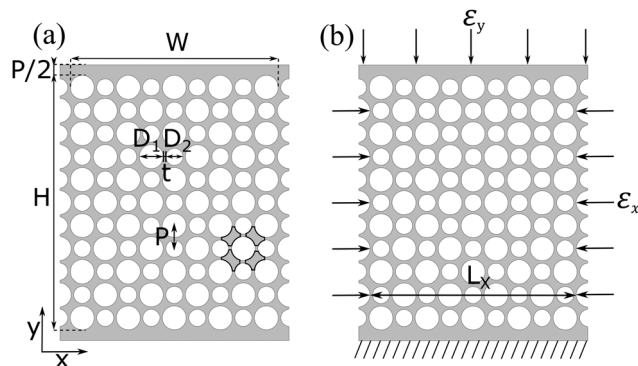

Fig. 1 (a) Schematic of the biholar domain: H and L denote the effective dimensions, $D_1 = 10$ mm and $D_2 = 7$ mm are the diameters of the large and the small holes, $P = 10$ mm is the distance between the centers of the holes, and $t = 1.5$ mm is the thickness of the filaments. The four black boundaries depict primitive rectangles of the underlying mechanism.[31] (b) Schematic of applied loadings: a preload is first applied to even rows by enforcing a horizontal strain ε_x followed by a uniaxial loading ε_y applied on the top of the sample while keeping the bottom fully constrained.

Elite Double 8 silicone rubber, and report results from two types of soft partitions, among others we investigated.

In the first, namely *equally spaced layer partition*, we embed two layers of soft inclusions (Fig. 2a) that define 3 regions, as shown in Fig. 2b and c, the latter depicting the manufactured specimen. Fig. 2d is a sketch of the structural analog we adopt in our analysis, where each biholar region is condensed into a biholar unit and connected in series to the adjacent through layers of soft inclusions. In the second partition, namely the *cross partition*, we embed a cross of soft inclusions (Fig. 2e), defining 5 regions in the geometric domain of Fig. 2f and the manufactured specimen of Fig. 2g. The partition possesses a central symmetry centered at point O (Fig. 2f). Analogous to Fig. 2d, Fig. 2h depicts our structural analog where soft inclusions form a cross segregating and connecting condensed biholar units at five locations, 4 cross-bracing and one central.

3. Experimental and numerical methods

3.1. Experimental methods

Our samples are manufactured by pouring Zhermack Elite Double 8 ($E = 220$ kPa, $\nu = 0.5$) into a mold 3D-printed using Ultimaker PLA filament ($E = 2.3$ GPa) and a commercial 3D printer (Ultimaker 3). After manufacturing, we carefully removed any rubber sliver arising from the molding process. The samples are 40 mm thick to prevent out-of-plane buckling and were tested a week after manufacturing allowing the completion of the aging process and the stabilization of the material properties.

To apply lateral confinement, we glued 1/16″ ER308L weld wire electrode bars of 50 mm length at the even edges of the sample and inserted laser cut 1.5 mm plexiglass plates in each face of the sample to constrain the positions of the bars at desired levels of confinement. The specimens were tested
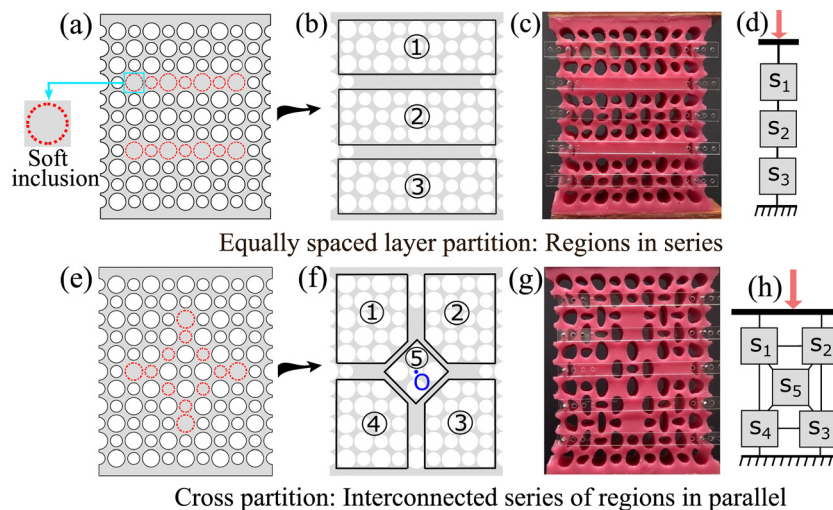
Fig. 2 Systems of soft inclusions forming two types of partitions: (a) design domain of equally spaced layer partition enabling the separation of (b) three regions in series; (c) manufactured sample and (d) corresponding analog model with three mechanical units in series. (e) Design domain of cross partition defining (f) 5 regions with central symmetry centered at point o; (g) manufactured sample and (h) relative analog model comprising interconnected series of mechanical units in parallel.

under uniaxial compression–decompression loading using an Admet (model eXpert 5000, MA, USA). To clamp specimens, we glued them onto wooden clamps that were fixed to the tester fixtures.

Our experimental acquisition protocol involves measuring the force displacement while capturing snapshots of the deformed sample. We considered a moderate displacement rate equal to 0.1 mm s^{-1} to avoid any viscoelastic or creep effects that could stem from an overly slow or overly fast rate of the applied displacement. We used a 150 lbf load cell with a resolution above 10 mN to measure the force. During testing, snapshots of the samples were captured using a Sony RX 100 VII camera facing the samples. The snapshots and the testing machine data acquisition were synchronized at 2 Hz. A Wiener filter enabled the removal of noise from snapshots where we tracked the positions and the geometrical parameters of ellipses using MATLAB (R2020b, MA, USA).

3.2. Numerical methods

Nonlinear finite element analysis was carried out with the commercial software ABAQUS 2020 (Dassault Systèmes Simulia Corp) with Standard Implicit Dynamics solver and geometric nonlinearity (NLgeom). We used moderate dissipation to ensure convergency in the presence of contact. The rubber base material was modeled with a nearly incompressible neo-Hookean law described with the following energy function:

$$W = \frac{\mu}{2}\left(\det(\boldsymbol{F})^{-\frac{2}{3}}\text{tr}\left(\boldsymbol{F}\boldsymbol{F}^T\right) - 3\right) + \frac{K}{2}(\det(\boldsymbol{F}) - 1)^2$$

where μ is the shear modulus, K is the bulk modulus, and $\boldsymbol{F} = \frac{\partial \boldsymbol{x}}{\partial \boldsymbol{X}}$ is the deformation gradient tensor, $\boldsymbol{x}$ and $\boldsymbol{X}$ being the deformed and undeformed coordinates. We set material properties consistent with those experimentally measured

($\nu = 0.499$, $E = 220$ kPa). The structures were discretized with quadratic plane stress triangle elements CPS6, and a systematic mesh convergence enabled to reach a mesh size of $t/4$ allowing four elements in the thinnest filaments. The simulation is performed in two steps. The first consists of applying lateral confinement, tilting, and gravity forces to the specimen. The second step consists of applying uniaxial loading.

4. Weak interaction pathways in equally spaced layer partition

In this section, we examine pathways in the equally spaced layer partition, which corresponds to a metamaterial composed of units in series. We first explore the phenomena under uniform lateral confinement, study the impact of varying its level, then tune its level locally in given regions of the domain.

4.1. Collective buckling and sequential switch of polarization

To explore the phenomena occurring in the equally spaced layer partition, we apply a uniform confining strain $\varepsilon_x = 0.12$ to even rows of the metamaterial, followed by a uniaxial compression–decompression cycle (Fig. 3a). Fig. 3b shows the force–displacement curve obtained numerically (solid line) and experimentally. The dashed line corresponds to the response of a representative specimen and the shaded area to the dispersion of results. Fig. 3b shows that state (1) highlighted on the solid curve corresponds to the initial state of the experimental metamaterial under lateral confinement applied before the vertical compression; whereas states (2)–(4) and (5)–(7) correspond to instability events triggered by compression and decompression respectively. Snapshots of corresponding polarization distribution are represented in Fig. 3c where the color code corresponds to the intensity of the hole polarization.
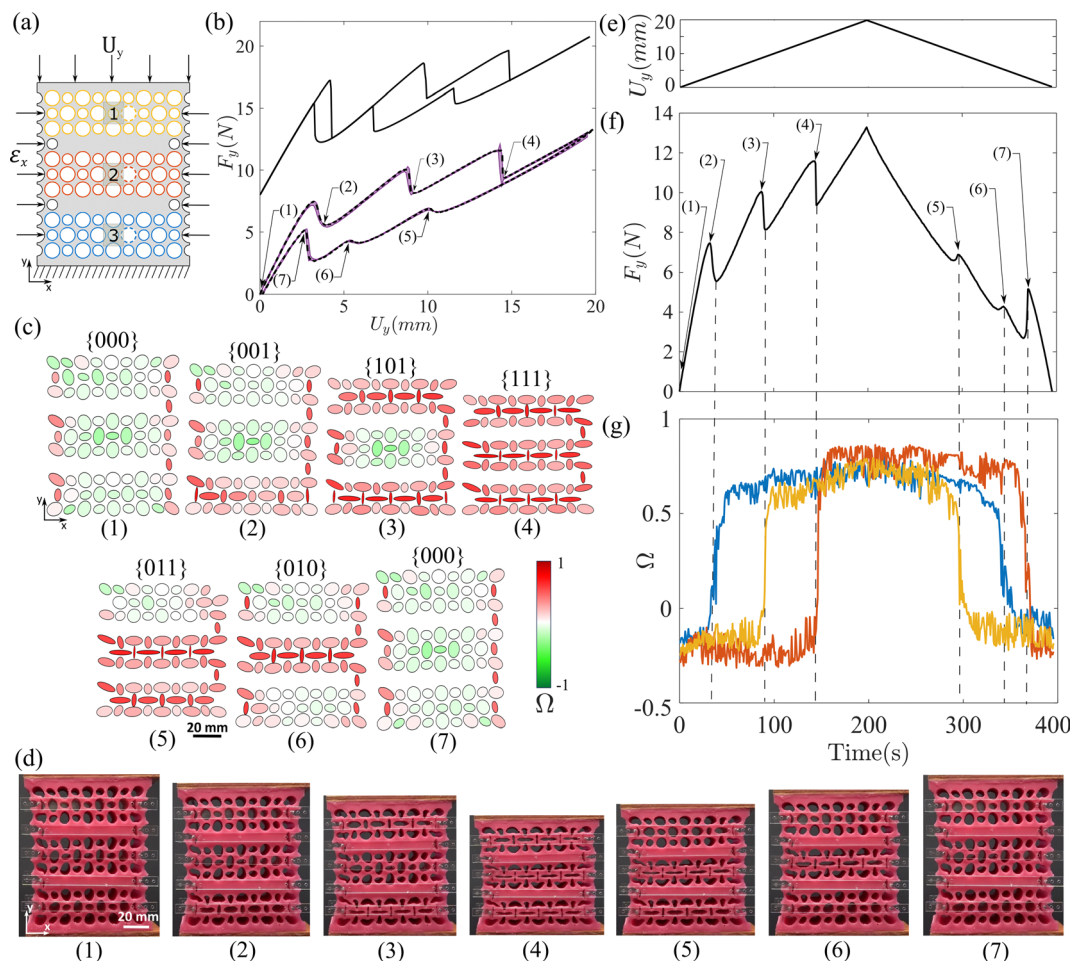
Fig. 3 (a) Schematic of the specimen under a horizontal confinement (ε_x) and a vertical displacement (U_y). Partition regions are highlighted in yellow (region 1), orange (region 2), and blue (region 3) with polarization holes (*i.e.*, where polarization is extracted) represented with dashed circles. (b) Force displacement curves – offset for clarity – for a confining strain $\varepsilon_x = 0.12$ obtained numerically (solid line) and experimentally. Dashed line displays the response of a representative specimen and filled area shows the dispersion of results. (c) Polarization distribution snapshots corresponding to (1)–(7) in the experimentally acquired force displacement curve with polarization colour code. Global state $S = \{s_1\, s_2\, s_3\}$, shown on the top of each snapshot: $s_i = 0$ for x-polarized state and $s_i = 1$ for y-polarized state where i = 1, 2, 3. (d) Experimental snapshots corresponding to (1)–(7). (e) Displacement U_y *versus* time curve (f) force time curve of the representative specimen showing three sharp jumps at compression and decompression. (g) Polarization as function of time in the experimental partition regions: yellow, orange, and blue curves correspond to yellow, orange, and blue regions.

We recall that the polarization of each hole is characterized by fitting an ellipse and is defined as $\Omega = \pm\left(1 - {p_2}/{p_1}\right)\cos(2\phi)$ where p_1 and p_2 are the major and minor axes respectively, and ϕ the angle between the major axis and the x-axis.[33] We set the polarization to be positive (y-polarized, red tint) when the major axis of the large ellipse is aligned with the x-axis, and to be negative when it is perpendicular to it (x-polarized, green tint). We observe a good agreement between the experimental and the numerical force–displacement curves. Deviations can be attributed to the manual application of lateral confinement, material stickiness, and sample imperfections rising from fabrication. Unlike an unbounded periodic lattice with perfect geometry, where instabilities occur randomly in the domain (see S1, ESI†), a partitioned lattice exhibits a sequence of regional and collective buckling of ligaments within each region (Fig. 3d), a behavior that is dependent on the asymmetry

of the applied preload. This leads to a sequential change of polarization in the partition regions (Fig. 3c) and to the observed drops/jumps in the solid curve in Fig. 3b.

Fig. 3f displays the force–time curve for a single compression–decompression cycle (Fig. 3e), where force drops (2–4) and jumps in force (5)–(7) are highlighted. The polarization in each partition region (yellow, orange, and blue regions in Fig. 3a) are represented with yellow, orange, and blue curves in Fig. 3g. Since the deformation is concentrated in the center of each region (Fig. 3c), the regional polarization curves (Fig. 3g) correspond to the polarization of the large hole located at the right of the central small hole of each region as pictured in Fig. 3a. The noise observed in the polarization curves is due to numerical artifacts during the tracking of ellipses positions and parameters. We can find that each force drop/jump in Fig. 3f corresponds to a sudden change of polarization in each partition region (Fig. 3g).

The polarization at a given time t can be represented by $\underline{\Omega}_t = \begin{pmatrix} \Omega_1 \\ \Omega_2 \\ \Omega_3 \end{pmatrix}_t$ where Ω_1, Ω_2, and Ω_3 represent the polarizations in regions 1, 2, and 3. Under uniform confinement, the specimen shows an x polarization (negative, green tint) throughout the domain (snapshot 1, Fig. 3c).

Initially, the polarization in the confined structure can be represented by $\underline{\Omega}_{t=0} = \begin{pmatrix} -0.25 \\ -0.29 \\ -0.21 \end{pmatrix}$. The polarization difference between regions can be attributed to the positioning of soft inclusions, the weight of the sample, and sample boundary conditions. Region 1 is characterized by its proximity to the location of the uniaxial load, while region 3 is distinguished by the clamped bottom layer. In contrast, region 2 is surrounded by two frustrated inclusion layers resulting in its greatest level of frustration.

The distribution of the polarization intensity is correlated with the sequence of polarization switches that occurs in the structure. Low polarized regions change polarization before their highly polarized counterparts as the level of frustration is lower in these regions and allows an easier polarization switch.

Under applied compression and due to gravity forces, region 3 changes polarization first (turning red, y-polarized) and generates a new polarization distribution (snapshot 2, Fig. 3c). Under continuous compression, the structure densifies leading to an increase in force as observed in Fig. 3f until region 1, which has a lower negative polarization than region 2, changes polarization (snapshot 3, Fig. 3c). Lastly, the highly polarized region 2 changes polarization leading to a y polarization (positive, red) throughout the domain (snapshot 4, Fig. 3c). Continuous compression makes the structure denser with a close and high polarization in the regions. Such sequence has been validated numerically (see S2 in the ESI†), for a prescribed level of preloading identical to that experimentally applied. On the other hand, if the simulation is performed without gravity, the outcome varies. Region 1 changes polarization prior to region 3 due to its proximity to the loading forces and the absence of body forces (see S2 in the ESI†).

Under decompression, the regions change polarization sequentially (snapshot 5-6-7, Fig. 3c) until reaching an x-polarized state where all regions show an x-polarization. Due to the location of the decompressing load, contact friction caused by densification, and frustration distribution, region 1 switches polarizations first, followed by region 3 and the highly frustrated region 2.

The mechanical characteristics of the metamaterial arise from the interplay between the intrinsic mechanism behaviour (represented by the rotating rectangle mechanism[33] shown in Fig. 1a) and conventional elasticity, which involves the bending and buckling of ligaments. As the domain size increases, there is a greater propensity for the mechanism behavior to diminish, resulting in the emergence of randomly distributed events of

distortion and localized buckling. For this reason, the study of regions of larger size is beyond the scope of this paper since it would cause inhomogeneities that no longer pertain to the study of hysterons in a mechanical metamaterial.

4.2. Hysteretic transitions and sequential pathways

As observed in the previous section, embedding soft inclusions leads to a spatially localized hysteretic change of polarization in each region of the partition for a confinement $\varepsilon_x = 0.12$. The hysteretic regions 1, 2, and 3 can, therefore, be considered as mechanical units with states denoted as s_1, s_2, and s_3. Each region i in $\{1, 2, 3\}$ possesses two distinct states: $s_i = 0$ for an x-polarized state and $s_i = 1$ for a y-polarized state. The whole specimen is characterized by a global state $S = \{s_1\ s_2\ s_3\}$, as reported at the top of each snapshot in Fig. 3c.

By tracking state changes and interactions, we can generate a directed graph that shows the deformation pathway in the metamaterial. This is shown in Fig. 4a. Here, the global states are represented by nodes (rounded rectangles), while the transition between them, under compression/decompression, is represented by red/blue arrows respectively. The color of the rectangle surrounding the global state specifies the color of the region where the change of polarization has occurred. The grey rectangle denotes the initial state.

For each region i in $\{1, 2, 3\}$, we denote the displacement threshold at the sudden change of polarization as U_i^+ for the hysteretic transition from state 0 to state 1 and as U_i^- for the transition from state 1 to state 0 (Fig. 4b). The hysteretic range $U_i^- < U < U_i^+$ corresponds to a state 0 or 1 and depends on the loading history. In our analysis, the main pathways (denoted as P^+ and P^-) are representative of the sequential transitions observed during compression (P^+) and decompression (P^-). We can describe this as a numerical list denoting the order of polarization changes within the regions enclosed in brackets (Fig. 4a).

For the structure in Fig. 3, starting from the initial state $\{000\}$, the continuous monitoring of force and polarization
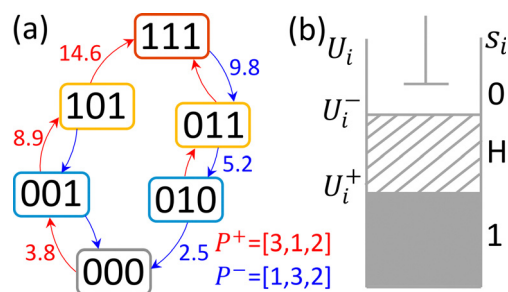

Fig. 4 (a) Transition graph for a confinement $\varepsilon_x = 0.12$ with 6 nodes representing the states. Transitions in compression (decompression) represented by red (blue) arrows. Main pathways in compression and decompression coded in red and blue respectively on the right of the graph and corresponding displacement thresholds displayed over the graph arrows. (b) Schematic of the mechanical unit with two states 0 (white) and 1 (grey). The dashed area corresponds to the hysteretic range $U_i^- < U_i < U_i^+$ ($i = 1, 2, 3$) where the state is either 0 or 1 depending on history.

shows the following sequence $\{001\} \rightarrow \{101\} \rightarrow \{111\}$, leading to $P^+ = [3,1,2]$ in compression. During decompression, the specimen starts from the fully y-polarized state $\{111\}$ and exhibits the following sequence: $\{011\} \rightarrow \{010\} \rightarrow \{000\}$, leading to $P^- = [1,3,2]$. Since weak interactions exist between the partition regions, the order of the switching events is independent of the state of other hysterons.

4.3. Impact of lateral confinement level

The previous section has shown that the incorporation of soft inclusions induced an uneven degree of frustration within the domain regions due to boundary conditions and weight, leading to a sequential change of polarization when subjected to a uniform confinement $\varepsilon_x = 0.12$. This section examines the impact of distinct levels of uniform confining strain on the force–displacement curves and sequential alterations in shape.

Fig. 5 illustrates the force–displacement curves pertaining to specific lateral confining strains, accompanied by snapshots of the specimen at given sample states. The corresponding pathways are depicted on the right-hand side of the curves. The polarization switch between the x and y states exhibits either non-hysteretic or hysteretic behavior contingent upon the magnitude of the lateral confinement. Non-hysteretic behavior is observed for lateral confinement $0 \leq \varepsilon_x < 0.08$, and hysteretic behavior is observed for lateral confinement $0.08 \leq \varepsilon_x \leq 0.18$.
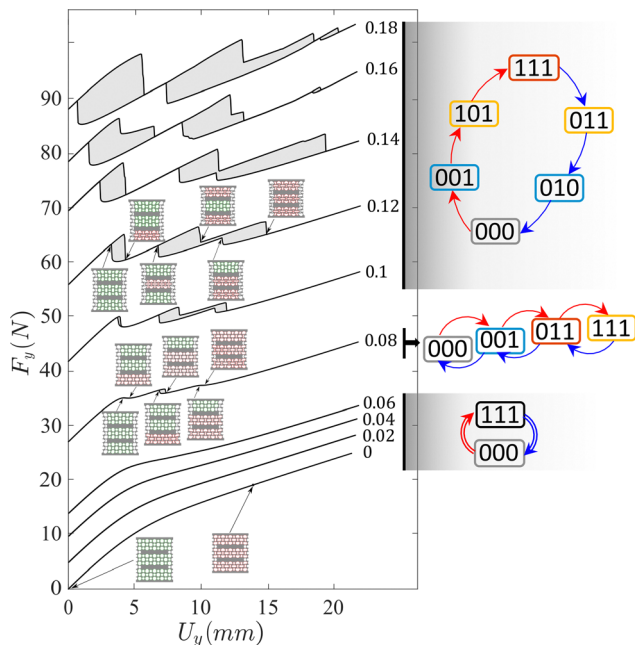

Fig. 5 Mechanical response of the equally spaced layer partition under increasing lateral confinement $\varepsilon_x = 0$ to 0.18, with discrete increment of 0.02. Non-hysteretic regime for $0 \leq \varepsilon_x < 0.08$ and hysteretic regime for $0.08 \leq \varepsilon_x \leq 0.18$, where grey shade indicates hysteresis. Curves are offset upward for clarity and are accompanied by snapshots of the specimen at given metamaterial states where x and y polarized holes are highlighted in green and red respectively. Transition graphs corresponding to confinement $0 \leq \varepsilon_x < 0.08$, $\varepsilon_x = 0.08$, and $0.08 < \varepsilon_x \leq 0.18$ are exhibited on the right-hand side. Double arrows indicate a simultaneous change of polarization in partition regions.

For $\varepsilon_x < 0.08$, the polarization switch is not sequential but occurs simultaneously and smoothly in all domain regions leading to a smooth shape transformation $\{000\} \rightarrow \{111\}$ represented with double arrows in Fig. 5. For $\varepsilon_x = 0.08$, the response is nonmonotonic and non-hysteretic for the first and third transitions but is hysteretic for the second transition as the most confined region leads to hysteresis, inducing the following pathways $\{000\} \rightarrow \{001\} \rightarrow \{011\} \rightarrow \{111\}$ and $\{111\} \rightarrow \{011\} \rightarrow \{001\} \rightarrow \{000\}$ during compression and decompression respectively.

The pathway that was observed in the previous section is obtained for $0.1 \leq \varepsilon_x \leq 0.18$. For $0.14 \leq \varepsilon_x \leq 0.18$, however, the force signal is characterized by the emergence of multiple peaks that are attributed to local instabilities resulting from the amplification of inhomogeneities caused by the high lateral confinement.

4.4. Tunable pathways through inhomogeneous confinement

Uniform confinement, when applied to even rows in our biholar domain, can generate a non-uniform level of frustration characterized by dissimilarity in the switching fields during compression and decompression. We now take a step forward to tune and program pathways by imposing a locally varying set of boundary conditions, where our baseline of comparison is the domain with uniform confinement $\varepsilon_x = 0.12$.

To generate non-uniform confinement, we prescribe a confining strain, $\varepsilon_x = 0.12$, to each row embedding soft inclusions, and enforce a selected strain ε_i (i in $\{1,2,3\}$) to the remaining biholar regions from the range $0.1 \leq \varepsilon_i \leq 0.14$ that has shown, in the previous section, to induce a hysteretic sequential response in the partitioned metamaterial without the emergence of inhomogeneities. We examine six cases (Fig. 6b). In the first three cases, we tune a single confining strain while in the other three cases, we apply distinct confining strains to each region. This results in six frustration distributions, each characterized by an initial polarization vector (Fig. 6b). The frustration distributions define six pathways, characterized by P^+ and P^-, as well as displacement thresholds U^+ and U^- in compression (red) and decompression (blue), represented at the bottom of each transition graph.

For the case $(\varepsilon_1, \varepsilon_2, \varepsilon_3) = \left(\varepsilon_x, \frac{5}{6}\varepsilon_x, \varepsilon_x\right)$, region 2 is the first to change polarization in compression as it becomes the least polarized followed by a change of polarization in region 3 and region 1, leading to $P^+ = [2,3,1]$. In decompression, there is a flip of the switching order of region 2 and region 3, leading to $P^- = [1,2,3]$.

For the case $(\varepsilon_1, \varepsilon_2, \varepsilon_3) = \left(\frac{7}{6}\varepsilon_x, \varepsilon_x, \varepsilon_x\right)$, where the confining strain of region 1 is increased, we observe a swap of the switching order of region 1 and 2, leading to $P^+ = [3,2,1]$. In decompression, a sequence like that of uniform confinement appears, leading to $P^- = [1,3,2]$.

The case $(\varepsilon_1, \varepsilon_2, \varepsilon_3) = \left(\varepsilon_x, \varepsilon_x, \frac{7}{6}\varepsilon_x\right)$ induces a gradient of frustration that increases from the location of applied load to the clamped bottom edge. This enables access to a large set of
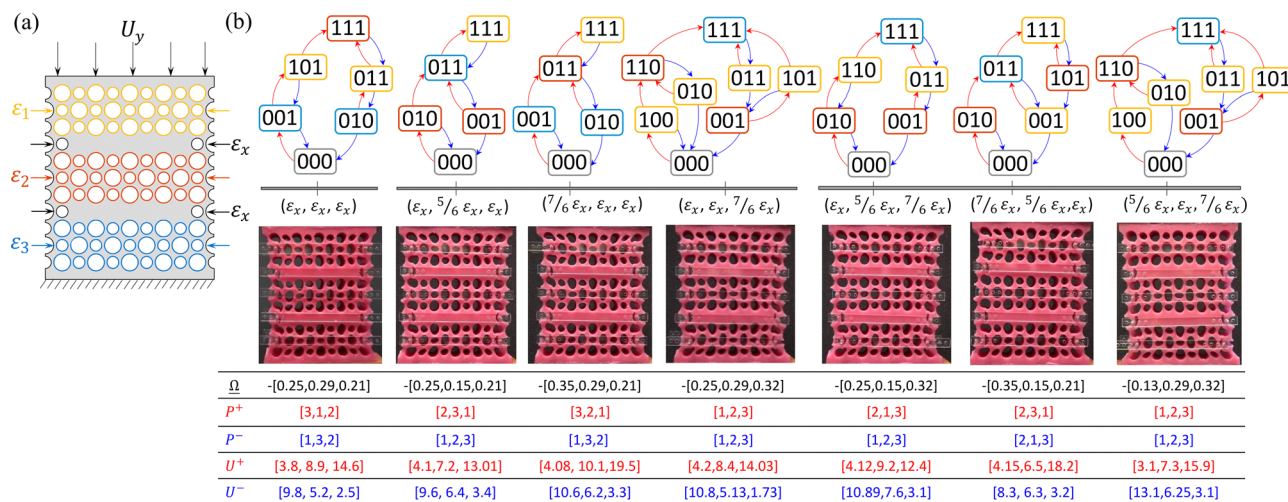
Fig. 6 (a) Schematic of the metamaterial with tuned regional confinement (ε_1, ε_2, ε_3): ε_i, i in {1, 2, 3}, expressed as function of ε_x. (b) Transition graphs for each heterogenous confinement case with transitions at compression (decompression) represented by red (blue) arrows. Initial polarization vectors, as well as main pathways, and corresponding displacement thresholds at compression and decompression depicted beneath each transition graph in red and blue respectively.

states (Fig. 6b), and programs the switching fields based on the regional frustration level, leading to $P^+ = P^- = [1,2,3]$.

In the first three cases, we tuned a single value of regional confining strain which resulted in a frustration distribution that induces frustration programmability in compression. This was altered at decompression due to contact friction[18] resulting from densification and to the location of decompressing load. In the next three cases (Fig. 6b), we apply distinct strains to the regions and showcase the programmability of the switching sequence with respect to the applied regional strains. This results in a heightened disparity in frustration between the regions, exceeding that observed in the preceding cases.

For $(\varepsilon_1, \varepsilon_2, \varepsilon_3) = \left(\varepsilon_x, \dfrac{5}{6}\varepsilon_x, \dfrac{7}{6}\varepsilon_x\right)$, we obtain the pathway $P^+ = [2,1,3]$. In decompression, however, the sequence is $P^- = [1,2,3]$.

For $(\varepsilon_1, \varepsilon_2, \varepsilon_3) = \left(\dfrac{7}{6}\varepsilon_x, \dfrac{5}{6}\varepsilon_x, \varepsilon_x\right)$, in compression, we obtain the following main pathway $P^+ = [2,3,1]$, whereas, in decompression, the sequence follows $P^- = [2,1,3]$ with the second region being the first to change polarization as region 1 possess a high frustration.

In the preceding two cases, the pathway could be programmed during compression by adjusting the strain level within each region. Nevertheless, the programmability during decompression is altered because of contact friction caused by densification as well as the location of the decompressing load.

In the last case of Fig. 6b, we program the pathway in compression and decompression by applying a gradient of lateral strains $(\varepsilon_1, \varepsilon_2, \varepsilon_3) = \left(\dfrac{5}{6}\varepsilon_x, \varepsilon_x, \dfrac{7}{6}\varepsilon_x\right)$. Applying an increasing lateral strain from the location of decompressing load to the clamped bottom edge induces $P^+ = P^- = [1,2,3]$.

While non-uniform confinement enables significant tuning of pathways in the metamaterial regions, the metamaterial with equally spaced layer partition exhibits weak interactions. To achieve strong interactions, we consider, in the next section, a

cross partition obtained by separating 5 regions using soft inclusions. Although the observed pathway depends on the asymmetry of the preloading and the interaction through the rotation of the central region, other strategies can be equally effective for pathway tuning, such as variations in the ligament thickness and other geometric parameters of the biholar lattice.

5. Strong interaction pathways

5.1. Protection, rotation, and symmetrical shape changes

To explore interactions between metamaterial regions, we need a partition with a stronger coupling between regions. Specifically, this requires that a change of state in one region results in a switch of state in another region.[20] To achieve this, we embed a cross of soft inclusions that divides the domain into 5 regions (Fig. 7a). Similar to the *equally spaced layer* partition, we subject the cross partition to a uniform confinement $\varepsilon_x = 0.12$. Since the specimen has a central symmetry, a $\theta_1 = -1°$ rotation is applied to the clamping stage at the bottom of the sample as shown in Fig. 7a during experiments and simulations to trigger the deformation from one side of the sample.

Fig. 7b shows the force–displacement curve obtained numerically (solid line) and experimentally. The dashed line corresponds to the response of a representative specimen and the shaded area to the dispersion of the results. We observe a good agreement between the force–displacement curves with deviations mainly arising from specimen imperfections, stickiness, and the manual application of confinement. Experimental snapshots of states (1–8) highlighted on the experimental curve and their corresponding polarization distribution snapshots are represented in Fig. 7c and d respectively. Similar snapshots were obtained numerically as shown in S3 in the ESI.†

Under applied compression and decompression (Fig. 7e), the confined specimen exhibits a sequence of regional and
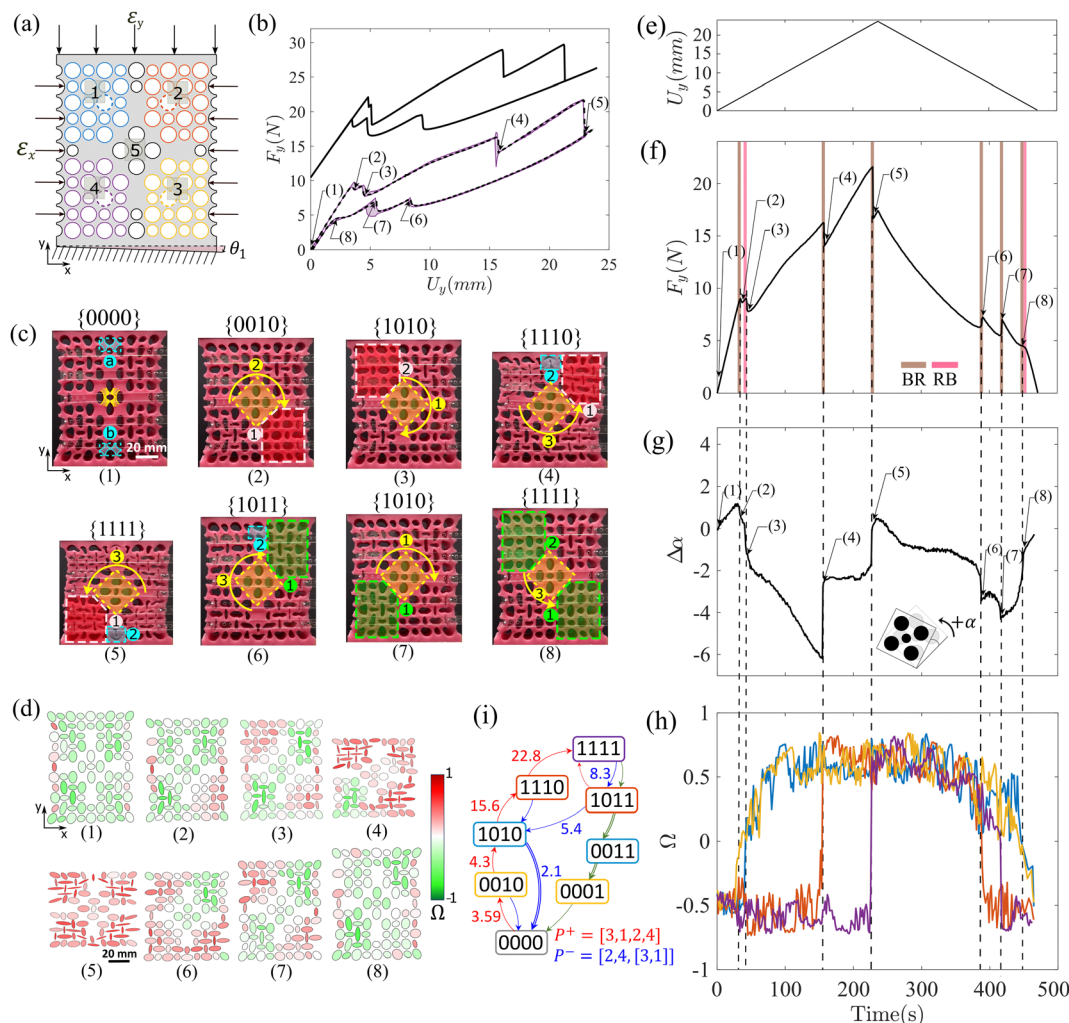
Fig. 7 (a) Schematic of the structure under applied loadings: horizontal confinement (ε_x), and vertical displacement (U_y). Cross partition regions highlighted in blue (region 1), orange (region 2), yellow (region 3), and purple (region 4) with central holes represented with dashed circles. (b) Force displacement curves for a confining strain $\varepsilon_x = 0.12$ obtained numerically (solid line) and experimentally. Dashed line displays the response of a representative specimen and filled area shows the dispersion of results. Curves are offset for clarity. (c) Experimental snapshots corresponding to (1)–(8) in the experimentally acquired force displacement curve. Protected mechanism in region 5 highlighted in yellow and snapping units a and b highlighted in blue in snapshot 1. Global state $S = \{s_1 s_2 s_3 s_4\}$, shown on the top of each snapshot: $s_i = 0$ for x-polarized state and $s_i = 1$ for y-polarized state where $i = 1$, 2, 3, 4. The sequence of subevents leading to each state is highlighted and numbered in each snapshot. (d) Snapshots of polarization distribution corresponding to (1)–(8) in the experimentally obtained force displacement curve with polarization colour code. (e) Displacement U_y versus time curve. (f) Force time curve obtained experimentally under uniaxial loading U_y. (g) Rotation angle of the protected region as function of time with arbitrary positive direction highlighted. (h) Polarization in the experimental partition regions as function of time: yellow, orange, blue, and purple curves correspond to yellow, orange, blue, and purple regions. (i) Transition graph with states represented by the nodes, and transitions in compression (decompression) represented by red (blue) arrows. Main pathways in compression and decompression coded in red and blue respectively on the right of the graph and corresponding displacement thresholds displayed over the arrows of the pathway. Pathway obtained for decompression from $U_y = 22.8$ coded in green.

collective buckling of ligaments within each region (Fig. 7c), leading to a sequential change of polarization in the partition regions (Fig. 7c and d), and to the observed drops/jumps in the force–time curve (Fig. 7f).

Since the central region (region 5, Fig. 7a) contains four large holes and one small hole, and is protected by a ring of soft inclusions, the square mechanism (highlighted in yellow in snapshot 1, Fig. 7c) is surrounded by a thick, soft layer, that lowers its deformation and polarization intensity, which inhibits its sudden change of polarization (Fig. 7c and d). However,

we observe that region 5 rotates with an angle that is plotted as a function of time in Fig. 7g. This result is obtained by tracking the orientation of the smallest square that can be enclosed at the boundaries of region 5. We arbitrarily set the rotation to be positive in the counterclockwise direction.

During the compression–decompression cycle, we observe a correlation between the abrupt polarization change of individual metamaterial regions and the sudden rotation of the protected region 5. The correlation is through two phenomena, a buckling-induced rotation (BR) and a rotation-induced

buckling (RB). The former describes the rotation of region 5 due to a change of polarization (highlighted in brown at force drops/jumps in Fig. 7f) and the latter describes the change of polarization due to a rotation of region 5 (highlighted in pink at force drops/jumps in Fig. 7f).

To track the shape changes in the remaining partition regions (blue, orange, yellow, and purple regions in Fig. 7a), Fig. 7h plots the polarization of the central large hole of each partition region (Fig. 7a) with blue, orange, yellow, and purple curves respectively. At a time, t, the metamaterial is characterized by $\underline{\Omega}_t = \begin{pmatrix} \Omega_1 \\ \Omega_2 \\ \Omega_3 \\ \Omega_4 \end{pmatrix}_t$ where Ω_1, Ω_2, Ω_3, and Ω_4 represent the polarization of regions 1, 2, 3, and 4, respectively. Due to the stage inclination, boundary conditions, and the self-weight of the sample, we initially observe close but non-uniform regional polarizations characterized by $\underline{\Omega}_0 = \begin{pmatrix} -0.43 \\ -0.46 \\ -0.39 \\ -0.48 \end{pmatrix}$.

Under uniaxial compression and due to geometric incompatibility generated by lateral confinement, region 3 which possesses the lowest polarization intensity, changes first polarization (jump 1 in Fig. 7h). This leads to the sudden rotation of region 5 in the clockwise direction (state 2, Fig. 7g and snapshot 2 in Fig. 7c) and to the drop in the force–time curve (state 2, Fig. 7f). In the presence of lateral confinement, the buckling induced rotation of region 5 (highlighted in brown in state 2 in Fig. 7f) changes the frustration distribution within the specimen causing the decrease of frustration in the centrally mapped region 1 and the rotation-induced change of its polarization (jump in the blue curve, Fig. 7h). The coupling between the change of polarization of region 1 and region 3 through the rotating region 5 shows the interaction between the two regions, which will be observed to be stronger during decompression due to friction. The RB event is correlated with the drop in force (state 3 highlighted in pink in Fig. 7f) and induces a symmetrical distribution of polarization around the central symmetry of the domain (snapshot 3 in Fig. 7c and d).

Further compression leads to a continuous rotation of region 5 in the clockwise direction and to the decrease of polarization of region 2 till its sudden change of polarization (jump in orange curve, Fig. 7h) and to the snapping of the ligaments in the connecting bi-square unit a (highlighted in blue in snapshot 1, Fig. 7c). Without this unit, the polarization change of region 2 is prevented and the rotation of region 5 in the negative direction would have continued, leading to the metamaterial densification. In contrast, the sudden change of polarization in region 2 leads to a sudden counterclockwise rotation of region 5 (state 4, Fig. 7g), to the third force drop in force (state 4 highlighted in brown, Fig. 7f), and to the snapshot 4 in Fig. 7c (highlighted in the snapshot are the sequence of events that occur in the structure).

Additional compression leads to a change of polarization of region 4 (jump in purple curve, Fig. 7h), causing the snapping of the bi-square unit b (also essential here for the same reasons explained for unit a), and the sudden counterclockwise rotation of region 5 (state 5, Fig. 7g). The sequence of subevents is highlighted in Fig. 7c (snapshot 5) and lead to the fourth force drop (state 5 highlighted in brown in Fig. 7f).

When we unload the metamaterial, the domain frustration decreases and region 5 smoothly rotates in the clockwise direction inducing a decrease of polarization of region 2 (located closer to the decompressing load), until it abruptly changes polarization (drop in orange curve, Fig. 7h). This results in the abrupt clockwise rotation of region 5 (state 6, Fig. 7g) and the force jump (state 6 highlighted in brown, Fig. 7f).

Further decompression causes a change of frustration in the centrally symmetric region 4 to region 2, which abruptly changes polarization (drop in the purple curve, Fig. 7h), resulting in a force jump (BR state 7 highlighted in brown, Fig. 7f) and a structure again with a centrally symmetric polarization distribution (snapshot 6, Fig. 7c). Continuous decompression causes a change in polarization of region 3 (drop in yellow curve in Fig. 7h) and its centrally symmetric region 1 (drop in blue curve in Fig. 7h), nearly simultaneously. This is due to the strong interaction between the two centrally symmetric regions which is more intense now due to friction in the dense structure.

5.2. Sequential pathways and impact of maximum loading displacement

The sudden and sequential change of polarization observed during the uniaxial compression–decompression cycle attests to the hysteretic nature of these regions, *i.e.*, they behave as hysteretic units with binary states denoted as s_1, s_2, s_3, and s_4. Similar to Section 4.2, we specify the global state of our specimen as $S = \{s_1 \; s_2 \; s_3 \; s_4\}$, and generate a transition graph that shows its sequential pathway (Fig. 7i) under a confinement $\varepsilon_x = 0.12$. Starting from the initial state $\{0000\}$, the continuous monitoring of force and polarization shows the following pathway $P^+ = [3,1,2,4]$ in compression. In decompression, the specimen starts from the fully y-polarized state $\{1111\}$ and exhibits the following sequence: $\{1111\} \rightarrow \{1011\} \rightarrow \{1010\} \rightarrow \{0000\}$, leading to $P^- = [2,4,[3,1]]$. The rotation-induced events, highlighted in pink in Fig. 7f, show an interaction between the centrally symmetric regions which is strong during decompression due to friction. Such transitions are depicted with double-blue arrows in Fig. 7i.

We notice that, if we unload as soon as state $\{1111\}$ is reached ($U_y = 22.8$), we observe a different sequence (highlighted in green in Fig. 7i): $\{1111\} \rightarrow \{1011\} \rightarrow \{0011\} \rightarrow \{0001\} \rightarrow \{0000\}$. Such discrepancies occur due to decreased contact when regions are less compressed and decreased central rotation. As a result, region 2, then region 1 change sequentially polarization, followed by its centrally symmetric region 3, then region 4. Discrepancies in the sequences $\{1011\} \rightarrow \{0011\}$ and $\{0011\} \rightarrow \{0001\}$ are highlighted with green double arrows in Fig. 7i.

5.3. Impact of lateral confinement

In this section, we examine the impact of distinct levels of uniform confining strain on the response of the cross partition. Fig. 8 illustrates the force–displacement curves for specific

lateral confining strains, accompanied by snapshots of the specimen at given states of the sample. The corresponding pathways are displayed on the right hand side of the curves. Depending on the value of the lateral confinement, the change of polarization between the x and the y states can be either non-hysteretic for $0 \leq \varepsilon_x < 0.08$, or hysteretic for $0.08 \leq \varepsilon_x \leq 0.16$.

For $\varepsilon_x < 0.08$, the change of polarization is not sequential but occurs simultaneously and smoothly in all domain regions. The corresponding transitions are highlighted with double arrows in Fig. 8. For $\varepsilon_x = 0.08$, the confinement is still minor therefore the region 4 with higher polarization changes first, leading to the slight rotation of the protected region 5, the sudden change of polarization of region 3, and to the first hysteresis in the force–displacement curve (Fig. 8). Regions 1 and 2, being less confined, change polarization in turn. This leads to the following sequence at compression: $\{0000\} \rightarrow$ $\{0001\} \rightarrow \{0011\} \rightarrow \{1111\}$. At decompression, region 1 and 2, the least confined and closest to the decompressing load, are the first to change polarization, followed by region 3 and region 4, leading to the sequence: $\{1111\} \rightarrow \{0011\} \rightarrow \{0001\} \rightarrow$ $\{0000\}$. For $\varepsilon_x = 0.1$, the change of polarization is hysteretic. Unlike $\varepsilon_x = 0.12$ (discussed previously), stronger interactions are observed between region 3 and region 1, which simultaneously change polarization, followed by region 4 and its centrally symmetric region 2. At decompression, we observe the following sequence: $\{1111\} \rightarrow \{1011\} \rightarrow \{1010\} \rightarrow \{0000\}$. For $\varepsilon_x = 0.14$, unit b becomes overly confined preventing the change of polarization in region 4 and leading to the sequences $\{0000\} \rightarrow$ $\{0010\} \rightarrow \{1010\} \rightarrow \{1110\}$ and $\{1110\} \rightarrow \{1100\} \rightarrow \{1000\} \rightarrow$ $\{0000\}$ at compression and decompression, respectively.

For $\varepsilon_x = 0.16$, unit a and unit b become both overly confined, preventing the change of polarization of regions 2 and 4. This
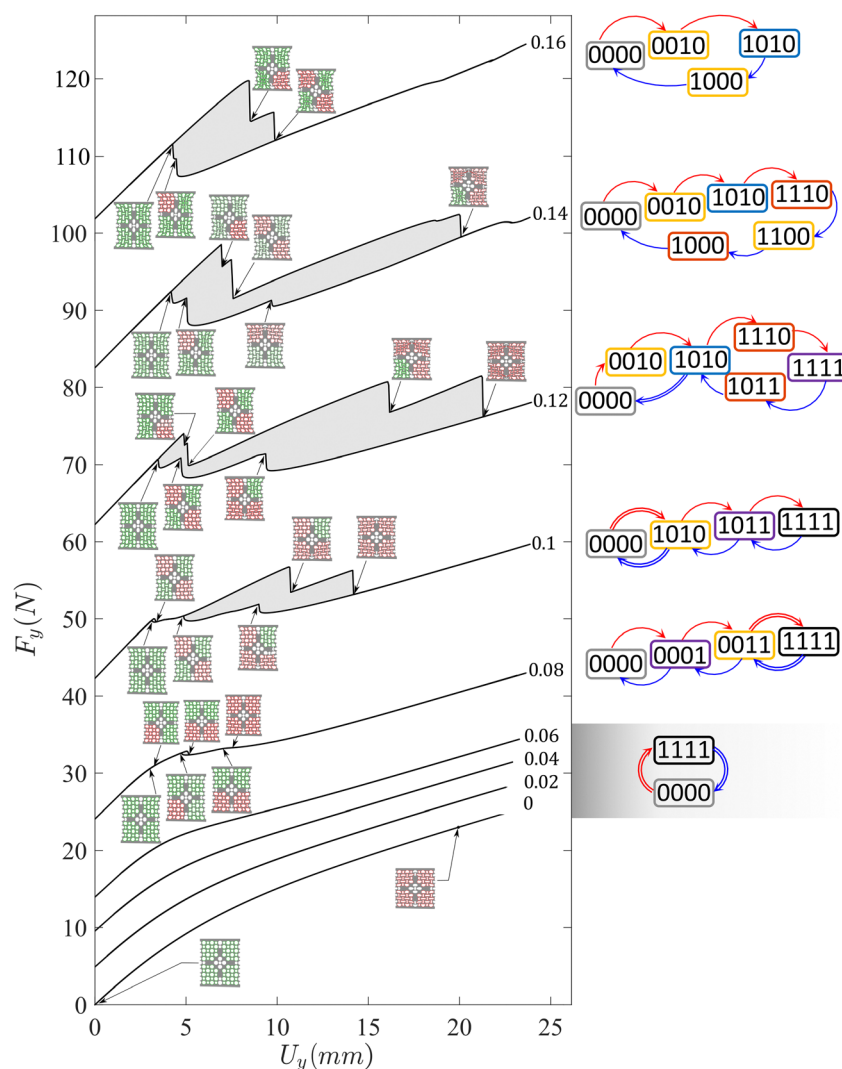

Fig. 8 Mechanical response of cross partition under increasing lateral confinement $\varepsilon_x = 0$ to 0.16 with a discrete increment of 0.02. Monotonic regime for $0 \leq \varepsilon_x < 0.08$ and hysteretic regime for $0.08 \leq \varepsilon_x \leq 0.16$, with hysteresis shaded in grey. Curves are offset upward for clarity and are accompanied by snapshots of the specimen at given metamaterial states where x and y polarized holes are highlighted in green and red respectively. Transition graphs corresponding to confinement $0 \leq \varepsilon_x < 0.08$, $\varepsilon_x = 0.08$, 0.1, 0.12, 0.14, and 0.16 are exhibited on the right-hand side. Double arrows indicate a simultaneous change of polarization in the partition regions.

leads to the sequences {0000} → {0010} → {1010} and {1010} → {1000} → {0000} at compression and decompression, respectively.

5.4. Impact of tilting and non-uniform lateral confinement

Pathways and interactions between regions can further be tuned if gradient of vertical prestrain as well as nonhomogeneous horizontal prestrain are applied to the metamaterial. The desired prestrains can be attained by modifying the inclination of one or two of the specimen boundaries in the case of the former prestrain, and by implementing non-uniform lateral confinement in the latter.

The lateral confinement is denoted by a set of three parameters $(\varepsilon_1, \varepsilon_2, \varepsilon_3)$, where ε_1 pertains to the uppermost layer, ε_2 to the three middle layers, and ε_3 to the lowermost layer, as illustrated in Fig. 9a. The variables ε_1, ε_2, and ε_3 are defined as a function of $\varepsilon_x = 0.12$. The lower and upper boundaries' inclinations are indicated by θ_1 and θ_2 (Fig. 9a), respectively, and are arbitrarily considered to be positively oriented in the counterclockwise direction. The process of preloading is succeeded by uniaxial compression and subsequent decompression.

We analyze a total of eight preloading cases (as depicted in Fig. 9b) and compare them to the baseline investigation that was previously conducted for a uniform confinement $\varepsilon_x = 0.12$ and $(\theta_1, \theta_2) = (0, -1)$. The different preloading scenarios lead to distinct distributions of frustration, each being characterized by an initial polarization vector, depicted underneath initial experimental snapshots in Fig. 9b. Eight pathways are characterized by distinct transition graphs in Fig. 9b. The main pathways, P^+ and P^-, as well as the displacement thresholds, U^+ and U^-, are shown in compression (red) and decompression (blue) underneath each transition graph (Fig. 9b).

The first four instances of preloading pertain to $(\theta_1, \theta_2) = (0, 10)$ which leads to a polarization switch of region 3 (shown in the four snapshots in Fig. 9b), and to distinct pathways depending on the applied lateral confinement.

For uniform and low confinement $(\varepsilon_1, \varepsilon_2, \varepsilon_3) = \frac{5}{6}(\varepsilon_x, \varepsilon_x, \varepsilon_x)$, regions 1 and 2 exhibit a similar low frustration while the frustration in region 4 differs due to the presence of tilting (Fig. 9b). As a result, the polarization switch of regions 1 and 2 takes place concurrently and is independent of the polarization switch in region 4, leading to the following pathway {0010} → {1110} → {1111} at compression and {1111} → {1110} → {0010} at decompression. Such decoupling between the upper and lower regions can also be observed for tilting $(\theta_1, \theta_2) = (0, -1)$ and in the presence of non-equal confinement between regions (1,2) and regions (3,4).

At higher confinement $(\varepsilon_1, \varepsilon_2, \varepsilon_3) = (\varepsilon_x, \varepsilon_x, \varepsilon_x)$, however, geometric incompatibility induces an increase in interaction between the centrally symmetric regions. The y-polarized state in region 3 induces a high polarization in region 1 (Fig. 9b), preventing its change of polarization and promoting only its densification during the compression–decompression cycle. On the other hand, region 4 and region 2 exhibit lower polarization and, under compression/decompression cycle, the least polarized region changes polarization first leading to {0010} → {0011} → {0111} in compression and to {0111} → {0011} → {0010} in decompression.

Applying $(\varepsilon_1, \varepsilon_2, \varepsilon_3) = \left(\frac{5}{6}\varepsilon_x, \varepsilon_x, \varepsilon_x\right)$ to the metamaterial induces less frustration in the upper layer of the metamaterial in comparison with the bottom layers. Under applied compression, the y-polarized region 3 densifies prompting the change of polarization of the centrally symmetric region 1 (which only densified in the previous case). This is succeeded by the change of polarization in region 4 and its centrally symmetric region 2, leading to the following pathway {0010} → {1010} → {1011} → {1111}. Under decompression, the centrally symmetric region 2 and region 4 change successively of polarization, followed by region 1, leading to the following pathway: {1111} → {1011} → {1010} → {0010}.
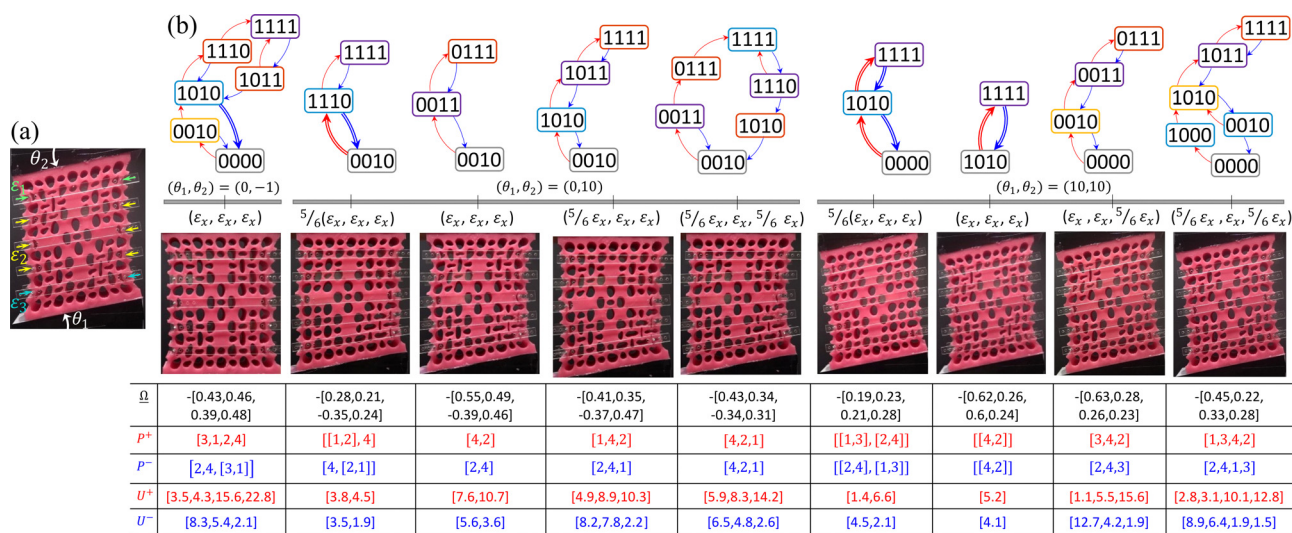

Fig. 9 (a) Metamaterial with tilted boundaries (θ_1, θ_2) and tuned lateral confinements $(\varepsilon_1, \varepsilon_2, \varepsilon_3)$ elicit distinct pathways represented by (b) transition graphs with transitions at compression (decompression) represented by red (blue) arrows. Initial polarization vectors, main pathways, and corresponding displacement thresholds at compression and decompression displayed under each pathway in red and blue, respectively.

For $(\varepsilon_1, \varepsilon_2, \varepsilon_3) = \left(\frac{5}{6}\varepsilon_x, \varepsilon_x, \frac{5}{6}\varepsilon_x\right)$, the regions change of polarization depending on their level of frustration. Region 4 is the least frustrated and changes polarization, followed by its centrally symmetric region 2, then region 1 which possesses the higher frustration, leading to the following pathway $\{0010\} \rightarrow \{0011\} \rightarrow \{0111\} \rightarrow \{1111\}$. During decompression, the switch also depends on the initial frustration distribution, leading to a change of polarization of region 4 followed by the change of polarization of region 2 and region 1.

In the next four cases, we apply a symmetric tilting characterized by $(\theta_1, \theta_2) = (10, 10)$ to amplify interactions among regions. In the first two cases, we study the impact of applying uniform confinement.

For $(\varepsilon_1, \varepsilon_2, \varepsilon_3) = \frac{5}{6}(\varepsilon_x, \varepsilon_x, \varepsilon_x)$ and under a large centrally symmetric tilting angle, centrally symmetric regions possess very close frustration, which is highly discernable between the pairs (Fig. 9b). This leads to an amplification of interaction between the centrally symmetric regions (1, 3) and (2, 4) and to their quasi-simultaneous change of polarization at compression and decompression. As a result, the following pathways emerge $\{0000\} \rightarrow \{1010\} \rightarrow \{1111\}$ and $\{1111\} \rightarrow \{1010\} \rightarrow \{0000\}$ in compression and decompression, respectively.

For a higher uniform confinement $(\varepsilon_1, \varepsilon_2, \varepsilon_3) = (\varepsilon_x, \varepsilon_x, \varepsilon_x)$, the polarization difference between region pairs intensifies and leads to the change of polarization of the least confined regions only, and to the densification of the highly frustrated regions. This leads to the pathways $\{0000\} \rightarrow \{1010\}$ and $\{1010\} \rightarrow \{0000\}$ at compression and decompression, respectively. The two previous cases attest that under large centrally symmetric tilting, uniform confinement leads to strong interactions between centrally symmetric regions.

In the next two cases, we explore the impact of non-uniform lateral confinement for the same tilting configuration.

For $(\varepsilon_1, \varepsilon_2, \varepsilon_3) = \left(\varepsilon_x, \varepsilon_x, \frac{5}{6}\varepsilon_x\right)$, region 1 becomes highly frustrated and therefore only densifies during compression. Because the four upper layers are more frustrated than the bottom layer, the transmission of deformation through the rotating region 5 decreases. As a result, the change of polarization occurs first in regions 3 and 4, and is decoupled from region 2, which is the last to change polarization. This leads to the following pathway $\{0000\} \rightarrow \{0010\} \rightarrow \{0011\} \rightarrow \{0111\}$ in compression and $\{0111\} \rightarrow \{0011\} \rightarrow \{0010\} \rightarrow \{0000\}$ in decompression.

For $\left(\frac{5}{6}\varepsilon_x, \varepsilon_x, \frac{5}{6}\varepsilon_x\right)$, we observe a similar pathway to the one observed for $(\varepsilon_1, \varepsilon_2, \varepsilon_3) = \left(\frac{5}{6}\varepsilon_x, \frac{5}{6}\varepsilon_x, \frac{5}{6}\varepsilon_x\right)$ with a difference: the change of polarization is distinct rather than quasi-simultaneous and induces the following pathways $\{0000\} \rightarrow \{1000\} \rightarrow \{1010\} \rightarrow \{1011\} \rightarrow \{1111\}$ in compression and $\{1111\} \rightarrow \{1011\} \rightarrow \{1010\} \rightarrow \{0010\} \rightarrow \{0000\}$ in decompression.

6. Conclusion

In this work, we introduced a system of experimentally observable hysterons in a large soft metamaterial by simply partitioning and frustrating a metamaterial domain. We first designed a biholar lattice beyond its conventional periodic arrangement of holes by embedding soft inclusions at strategic locations.

Sequential pathways are defined through the post-fabrication frustration of the partitioned metamaterial. We show that the response of the partitioned metamaterial is strongly dependent on the level of applied pre-strain which can generate distinct responses, from a smooth non sequential to a multi-step hysteretic response.

Unlike amorphous media[27,30,31] and crumpled sheets[27–29] where it is challenging to track pathways, this work has presented a straightforward strategy to track the deformation history and transition states in specific regions through the recording of regional polarization changes.

Partitioning enables tuning the sequential pathway from a longitudinal pathway with weak interactions *via an equally spaced layer partition* to a pathway with strong interactions triggered using a *cross partition* that exhibits protection and rotation of its central region rising from geometric incompatibility. Our work also emphasizes that a post-manufacture strategy that uses non-uniform lateral confinement and angle tuning of one or two of the clamping edges enables to tune the pathway as well as the intensity of regions interaction.

Overall, the results obtained in this paper rely on the asymmetry of loading induced from the lateral confinement, tilting, and gravitational forces applied to the specimen. Tuning the loading distribution enables to tune the switching fields in the partitioned regions and the resulting pathway as demonstrated both in our simulations (under ideal settings with neither manufacturing imperfections nor load misalignment), and experiments. The physics unveiled in this work as well as our experimental results are thus reproducible as long as (i) manufacturing-induced variations of the geometric parameters of the structure are minimized during fabrication and (ii) a proper application of loading is ensured with no misalignment between the specimen and the direction of the applied loading. Any deviations from the conditions described above can alter the observed pathways. Such sensitivity parallels that of a previous study[32] documenting the sensitivity of the uniaxial mechanical response of a periodic biholar metamaterial to variations of both filament thickness and hole diameters.

As works on experimentally observed pathways in more ordered systems start to emerge,[18,20] we hope that our work will open venues for the exploration of more complex pathways that can arise from the response of the base material including field responsivity and nonlinearity, such as plasticity. We also foresee that other methods for domain partitioning through the local change of geometric parameters, the design of complex patterns as well as the adoption of field responsive materials,[34–36] could enrich the design space and the range of attainable functionalities. Our strategy can be leveraged to partition the domain that makes up a soft machine,[37,38] hence holding the potential to expand the palette and complexity of motions currently achievable by existing soft robots.

Conflicts of interest

There are no conflicts to declare.

Acknowledgements

References

1 K. Bertoldi, P. M. Reis, S. Willshaw and T. Mullin, *Adv. Mater.*, 2009, **22**, 361–366.
2 A. Rafsanjani, A. Akbarzadeh and D. Pasini, *Adv. Mater.*, 2015, **27**, 5931–5935.
3 K. Bertoldi, *Annu. Rev. Mater. Res.*, 2017, **47**, 51–61.
4 K. Bertoldi, V. Vitelli, J. Christensen and M. van Hecke, *Nat. Rev. Mater.*, 2017, **2**, 17066.
5 D. M. Kochmann and K. Bertoldi, *Appl. Mech. Rev.*, 2017, **69**, 50801–50824.
6 A. Rafsanjani, L. Jin, B. Deng and K. Bertoldi, *Proc. Natl. Acad. Sci. U. S. A.*, 2019, 201817763.
7 L. Jin, R. Khajehtourian, J. Mueller, A. Rafsanjani, V. Tournat, K. Bertoldi and D. M. Kochmann, *Proc. Natl. Acad. Sci. U. S. A.*, 2020, **117**, 2319 LP–2325.
8 N. Nadkarni, A. F. Arrieta, C. Chong, D. M. Kochmann and C. Daraio, *Phys. Rev. Lett.*, 2016, **116**, 244501.
9 B. Deng, S. Yu, A. E. Forte, V. Tournat and K. Bertoldi, *Proc. Natl. Acad. Sci. U. S. A.*, 2020, 202015847.
10 Y. Cho, J.-H. Shin, A. Costa, T. A. Kim, V. Kunin, J. Li, S. Y. Lee, S. Yang, H. N. Han, I.-S. Choi and D. J. Srolovitz, *Proc. Natl. Acad. Sci. U. S. A.*, 2014, **111**, 17390 LP–17395.
11 A. Rafsanjani and D. Pasini, *Extrem. Mech. Lett.*, 2016, **9**, 291–296.
12 S. Shan, S. H. Kang, J. R. Raney, P. Wang, L. Fang, F. Candido, J. A. Lewis and K. Bertoldi, *Adv. Mater.*, 2015, **27**, 4296–4301.
13 M. Mungan, *Proc. Natl. Acad. Sci. U. S. A.*, 2022, **119**, e2208743119.
14 T. Chen, M. Pauly and P. M. Reis, *Nature*, 2021, **589**, 386–390.
15 C. El Helou, B. Grossmann, C. E. Tabor, P. R. Buskohl and R. L. Harne, *Nature*, 2022, **608**, 699–703.
16 L. J. Kwakernaak and M. van Hecke, *arXiv*, Prepr. arXiv2302.06947.
17 C. Coulais, A. Sabbadini, F. Vink and M. van Hecke, *Nature*, 2018, **561**, 512–515.
18 J. Ding and M. van Hecke, *J. Chem. Phys.*, 2022, **156**, 204902.
19 Z. Meng, M. Liu, H. Yan, G. M. Genin and C. Q. Chen, *Sci. Adv.*, 2022, **8**, eabn5460.
20 H. Bense and M. van Hecke, *Proc. Natl. Acad. Sci. U. S. A.*, 2021, **118**, e2111436118.
21 F. Preisach, *Zeitschrift für Phys.*, 1935, **94**, 277–302.
22 G. Mörée and M. Leijon, *Materials*, 2023, 16.
23 M. van Hecke, *Phys. Rev. E*, 2021, **104**, 54608.
24 I. Regev, I. Attia, K. Dahmen, S. Sastry and M. Mungan, *Phys. Rev. E*, 2021, **103**, 62614.
25 C. W. Lindeman and S. R. Nagel, *Sci. Adv.*, 2021, 7, eabg7133.
26 M. Adhikari and S. Sastry, *Eur. Phys. J. E*, 2018, **41**, 105.
27 Y. Lahini, O. Gottesman, A. Amir and S. M. Rubinstein, *Phys. Rev. Lett.*, 2017, **118**, 85501.
28 D. Shohat, D. Hexner and Y. Lahini, *Proc. Natl. Acad. Sci. U. S. A.*, 2022, **119**, e2200028119.
29 K. Matan, R. B. Williams, T. A. Witten and S. R. Nagel, *Phys. Rev. Lett.*, 2002, **88**, 76101.
30 N. C. Keim, J. Hass, B. Kroger and D. Wieker, *Phys. Rev. Res.*, 2020, **2**, 12004.
31 J. D. Paulsen, N. C. Keim and S. R. Nagel, *Phys. Rev. Lett.*, 2014, **113**, 68301.
32 B. Florijn, C. Coulais and M. van Hecke, *Soft Matter*, 2016, **12**, 8736–8743.
33 B. Florijn, C. Coulais and M. van Hecke, *Phys. Rev. Lett.*, 2014, **113**, 175503.
34 H. Yasuda, L. M. Korpas and J. R. Raney, *Phys. Rev. Appl.*, 2020, **13**, 54067.
35 L. M. Korpas, R. Yin, H. Yasuda and J. R. Raney, *ACS Appl. Mater. Interfaces*, 2021, **13**, 31163–31170.
36 X. Liang, H. Fu and A. J. Crosby, *Proc. Natl. Acad. Sci. U. S. A.*, 2022, **119**, e2118161119.
37 D. Yang, B. Mosadegh, A. Ainla, B. Lee, F. Khashai, Z. Suo, K. Bertoldi and G. M. Whitesides, *Adv. Mater.*, 2015, **27**, 6323–6327.
38 J. Zhang, Z. Ren, W. Hu, R. H. Soon, I. C. Yasa, Z. Liu and M. Sitti, *Sci. Robot.*, 2021, **6**, eabf0112.